

Layer-engineered quantum anomalous Hall effect in twisted rhombohedral graphene family

Zhangyuan Chen^{1,2*}, Naitian Liu^{1,2*}, Jiannan Hua^{1,2*}, Hanxiao Xiang^{1,2}, Wenqiang Zhou^{1,2}, Jing Ding^{1,2}, Xinjie Fang^{1,2}, Linfeng Wu^{1,2}, Le Zhang^{1,2}, Qianmei Chen³, Xuanyu Chen³, Kenji Watanabe⁴, Takashi Taniguchi⁵, Na Xin³, Wei Zhu^{1,2†}, Shuigang Xu^{1,2†}

¹ Key Laboratory for Quantum Materials of Zhejiang Province, Department of Physics, School of Science, Westlake University, Hangzhou 310030, China

² Institute of Natural Sciences, Westlake Institute for Advanced Study, Hangzhou 310024, China

³ Department of Chemistry, Zhejiang University, Hangzhou 310058, China

⁴ Research Center for Electronic and Optical Materials, National Institute for Materials Science, Tsukuba 305-0044, Japan

⁵ Research Center for Materials Nanoarchitectonics, National Institute for Materials Science, Tsukuba 305-0044, Japan

*These authors contributed equally to this work.

†Corresponding authors: zhuwei@westlake.edu.cn (W.Z.); xushuigang@westlake.edu.cn (S.X.)

Abstract

The quantum anomalous Hall (QAH) insulator is uniquely characterized by the topological Chern number C . Controlling the Chern number is a key step toward functional topological electronics and enables access to exotic quantum phases beyond the traditional quantum Hall physics. Here, we report a series of QAH insulators in twisted rhombohedral graphene family, in which the Chern number can be tuned through layer configuration, *in-situ* electrostatic doping, and displacement field. Specifically, in twisted monolayer-rhombohedral N -layer graphene, denoted as $(1+N)$ L, we observe QAH states with $C = N$ at moiré filling $\nu = 1$, where $N = 3, 4, 5$ represents the layer number of rhombohedral graphene. These results are experimentally confirmed by quantized Hall resistance and the Streda formula. In twisted monolayer-trilayer graphene, we also observe states with $|C| = 3$ at $\nu = 3$, whose sign can be switched by either electrostatic doping or displacement field. Furthermore, in twisted Bernal bilayer-rhombohedral tetralayer graphene denoted as $(2+4)$ L, we demonstrate a displacement-field-driven topological phase transition between two distinct QAH states with $C = 3$ and $C = 4$ at $\nu = 1$. Our work establishes twisted rhombohedral graphene as a highly versatile, layer-engineered platform for designing and dynamically controlling high-Chern-number topological matters.

The quantum anomalous Hall (QAH) effect, which exhibits a quantized Hall resistance of $R_{xy} = h/Ce^2$ and vanishing longitudinal resistance in the absence of an external magnetic field (B), represents a landmark achievement in topological physics and offers a promising route for low-power-consumption electronics [1,2]. The Chern number C not only characterizes the bulk topology of QAH insulators but also dictates the number of dissipationless chiral edge channels [3]. The pursuit of topological materials hosting high and gate-tunable C is thus crucial for advancing topological electronics, as it would enable multi-channel quantum transport, the investigation of topological phase transitions, and the exploration of exotic fractional topological states [4-8]. While the QAH effect has been realized in several materials, such as magnetically doped topological insulators [2], intrinsic magnetic topological insulators [9,10], and moiré systems [11-16], most of them exhibit a Chern number of $|C| = 1$. Tunable- C QAH can be achieved by stacking decoupled $C = 1$ QAH multilayers separated by normal insulator spacers [17]. However, experimental access to designed QAH states with intrinsic high- C topological bands remains elusive.

Rhombohedral multilayer graphene has emerged as a promising platform for engineering various QAH states, owing to its layer-dependent band topology [18-20]. Furthermore, its intrinsic layer-dependent surface flat bands, which follow an approximate energy dispersion relation of $E \sim k^N$ (where N is the layer number), host rich correlated topological phases due to the interplay between strong electron correlations and topological band structures [21-27]. Indeed, various topological states, including integer and fractional QAH effects, have been reported in rhombohedral graphene systems [15,28-30]. Much attention has focused on moiré superlattices formed by aligning rhombohedral graphene with hexagonal boron nitride (h-BN) [15,30-33]. Although theoretical calculations suggest that the valley Chern number of rhombohedral graphene scales with its layer number [19,34-36], experimental results consistently show Chern bands with $C = 1$ in rhombohedral graphene/hBN moiré systems, largely independent of the graphene layer number [15,30-32,37,38]. In contrast, very recent advances in twisted homostructures of rhombohedral graphene moiré superlattices indicate that they provide a more tunable alternative for exploring high- C QAH states [39-41].

In this work, we report the experimental realization of layer-engineered, high- C QAH insulators in a series of twisted rhombohedral graphene homostructures. Through systematic studies of twisted monolayer-rhombohedral N -layer (denoted as $(1 + N)$ L) graphene and twisted Bernal bilayer-rhombohedral tetralayer (denoted as $(2 + 4)$ L) graphene, we demonstrate three key advances. First, we observe the predicted layer-dependent Chern number of $C = N$ in twisted $(1 + N)$ L graphene family with $N = 3, 4, 5$. All members exhibit unambiguous QAH effects. Second, beyond tunability via layer number, we also find that the chirality of the QAH state (the sign of C) can be switched by both carrier density (n) and displacement field (D). Third, in twisted $(2 + 4)$ L graphene, we demonstrate a displacement-field-induced topological phase transition between two distinct QAH states with $C = 3$ and $C = 4$, showcasing the flexibility of engineering topological states in this platform.

Layer-dependent Chern bands

Our devices are fabricated using a van der Waals assembly technique, where a monolayer (or bilayer) graphene is placed on top of a rhombohedral multilayer graphene with a controlled small twist angle

θ , achieved via a standard cut-and-stack process [42,43]. The stack is fully encapsulated by top and bottom h-BN dielectrics, along with dual-graphite gates for independent electrostatic control. Throughout assembly, graphene is intentionally misaligned with the h-BN to avoid introducing additional moiré structures. The presence of rhombohedral stacking domains in the final stacks is confirmed by Raman mapping (see Methods and Extended Data Fig. 1). Figure 1a illustrates the device architecture of the twisted $(M + N)$ L graphene family. This dual-gate configuration allows for independent tuning of the n and D . The formation of a moiré superlattice in our homostructures is evidenced by the observation of resistivity peaks at full band filling ($\nu = 4$), from which θ is determined and cross-verified via Brown-Zak oscillations (see Methods and Extended Data Fig. 3).

The band structures for the twisted $(1 + N)$ L graphene, obtained from self-consistent Hartree-Fock calculations based on the continuum model, confirm that the first conduction band is an isolated topological flat band. This band carries a nonzero valley Chern number C that matches the layer number N , where $N = 3, 4, 5$ (see Fig. 1b). An optimized interlayer potential Δ can be experimentally achieved by tuning D . Strong Coulomb interactions within this isolated flat band are expected to lift the degeneracy of spin and valley flavors, leading to a spin- and valley-polarized orbital Chern band at odd integer moiré fillings [44,45]. Experimentally, by utilizing the dual-gate structure as illustrated in Fig. 1a, we tune the Fermi level to these odd ν to access the corresponding topologically nontrivial states with $C = N$.

Figure 1c presents representative magnetic hysteresis loops measured at one electron per moiré unit cell ($\nu = 1$) in three devices: twisted monolayer-trilayer ((1 + 3) L, device D1, $\theta = 1.29^\circ$), monolayer-tetralayer ((1 + 4) L, device D2, $\theta = 1.16^\circ$), and monolayer-pentalayer ((1 + 5) L, device D3, $\theta = 1.39^\circ$) graphene. All three devices exhibit a typical QAH effect, characterized by a quantized Hall resistivity $\rho_{xy} = h/Ce^2$ and a vanishing longitudinal resistivity ρ_{xx} down to zero magnetic field. The measured quantized plateaus of ρ_{xy} in device D1, D2, and D3 are $h/3e^2$, $h/4e^2$, and $h/5e^2$, respectively. The observation of QAH states with $C = N$ directly confirms the layer-dependent Chern number predicted by our band calculations and stems from the intrinsic, layer-dependent Berry curvature of rhombohedral graphene [46].

QAH at $\nu = 1$ in twisted (1 + 3) L and (1 + 4) L graphene

The full $\nu - D$ map of ρ_{xx} at $B = 0$ T for all devices are provided in Extended Data Fig. 2. In all cases, QAH states emerge when electrons are polarized away from moiré interface by applying a sufficiently large negative D . This behavior aligns with prior reports and is analogous to observations in rhombohedral graphene/h-BN systems [15,39].

Detailed measurements near $\nu = 1$ for twisted (1 + 3) L (device D1) and (1 + 4) L (device D2) graphene are shown in Fig. 2a-d and 2e-h, respectively. Figure 2a (2e) present fine $\nu - D$ maps of the symmetrized ρ_{xx} and anti-symmetrized ρ_{xy} , measured under a small magnetic field of $B = \pm 0.1$ T (± 90 mT), in order to stabilize the spontaneous magnetization. In Fig. 2a (device D1), clear minima in ρ_{xx} are observed within the D range of $-0.540 < D < -0.420$ V nm $^{-1}$, accompanied by maxima in ρ_{xy} . Similar features appear in Fig. 2e (device D2) for $-0.700 < D < -0.470$ V nm $^{-1}$. These signatures are characteristic of topologically nontrivial states. The higher $|D|$ required to observe the nontrivial states in (1 + 4) L graphene device, compared to the (1 + 3) L graphene

device, may be attributed to the enhanced interlayer screening effect in thicker graphene, as demonstrated in previous studies [26].

The presence of QAH states at optimized position is further verified by measuring ρ_{xx} and ρ_{xy} as a function of ν at fixed D (Fig. 2c, g) and as a function of D at fixed ν (Fig. 2d, h). Well-defined plateau in ρ_{xy} are observed together with vanishing ρ_{xx} . The quantized values are $h/3e^2$ for the (1+3) L device and $h/4e^2$ for the (1+4) L device, consistent with the results in Fig. 1c. The Chern number can also be alternatively extracted via the Streda formula, $\frac{\partial n}{\partial B} = C \frac{e}{h}$, by analyzing the Landau fan diagrams from magnetic field-dependent transport. As shown in Fig. 2b and 2f, the slope of these dispersive fan diagrams yields $C = 3$ for the (1 + 3) L device and $C = 4$ for (1 + 4) L device, further confirming the corresponding topological state in each case. The QAH effects in our devices are robust, with the decent quantization persisting up to 3 K and Cuire temperature reaching approximately 8 K (see Extended Data Fig. 4).

Beyond the conventional QAH effect at the integer filling $\nu = 1$, we observe that anomalous ρ_{xy} extends into neighboring non-integer filling ranges: for the (1 + 3) L device in the region $1 < \nu < 1.6$, and for the (1 + 4) L device in $0.6 < \nu < 1$ and $1 < \nu < 1.8$, as shown in Fig. 2a,e. Notably, at $\nu = 3/2$, the signature of a Chern insulator with $C = 2$ is identified (see Extended Data Fig. 8), indicating an interaction-induced doubling of the moiré unit cell [47]. This unconventional Chern insulator suggests that simultaneous breaking of both time-reversal and discrete translational symmetries, likely originating from topological charge order [16,47].

Switchable chirality at $\nu = 3$ in twisted (1 + 3) L graphene

In addition to the QAH effect at $\nu = 1$, we observe QAH states near $\nu = 3$ with $|C| = 3$ in the twisted (1 + 3) L device (device D1), as summarized in Fig. 3. Intriguingly, the chirality, namely the sign of C , can be effectively switched by either electrostatic doping (effectively the moiré filling factor ν) or the displacement field D .

Figure 3a-d display the $\nu - D$ map of ρ_{xx} and ρ_{xy} near $\nu = 3$ with ν swept forward and backward, measured under a small magnetic field of $B = 0.1$ T. A QAH state with $C = -3$ is identified at $\nu = 2.905$ and $D = -0.317$ V nm⁻¹, as confirmed by the magnetic hysteresis loop showing a quantized Hall plateaus at $-h/3e^2$ (Fig. 3g, left panel) and by Landau fan diagrams consistent with $C = -3$ via the Streda formula (Fig. 3e, f). Strikingly, similar QAH state but with opposite chirality, namely $C = 3$, can be also found at $\nu = 2.947$ and $D = -0.310$ V nm⁻¹ (Fig. 3g, right panel). Notably, the precise quantization of ρ_{xy} in both states persists down to zero magnetic field.

The $\nu - D$ maps measured at fixed small B in Fig. 3b and 3d reveal the coexistence of both large positive and negative ρ_{xy} , each corresponding to a minimum in ρ_{xx} (Fig. 3a, c). The boundary between these regions is sharp and depends on both ν and D . Comparing Fig. 3b with 3d, it is obvious that the direction of the ν scan alters the spatial distribution of positive and negative ρ_{xy} domains. A similar dependence on the D scan direction is also observed (Extended Data Fig. 6). This sensitivity of the ρ_{xy} sign to scan history manifests directly as prominent hysteresis when plotting ρ_{xy} versus ν (Fig. 3h) or versus D (Fig. 3i). Importantly, ρ_{xy} in both Fig. 3h and Fig. 3i

remains quantized at either $h/3e^2$ or $-h/3e^2$ before and after these switches. Consequently, in our device D1, the chirality of the QAH state near $\nu = 3$ can be controllably switched by three independent parameters: B , ν and D .

Electrostatic-doping-induced sign reversal of ρ_{xy} has been reported previously in twisted monolayer-bilayer graphene and related systems [29,32,48]. This behavior is a hallmark of orbital Chern insulators, where the total magnetization comprises contributions from both the bulk orbital magnetization and the chiral edge orbital current [49]. Sweeping the doping level across the Chern insulator gap can cause the edge-state contribution to dominate, reversing the total magnetization. Since the K and K' valleys carry opposite orbital magnetization due to their opposite valley Chern numbers, a sign change in the total magnetization drives a switch in the valley polarization. As a result, the Chern number of orbital Chern insulator, and thus the sign of the quantized ρ_{xy} , is reversed.

As shown in Fig. 3h, the ν -induced switching between opposite quantized ρ_{xy} values occurs at the same ν , forming a nearly rectangular hysteresis loop. Beyond the loop, ρ_{xy} deviate from the quantized values. In contrast, the D -induced switching between opposite quantized ρ_{xy} values (Fig. 3i) spans a broader range and can occur over different D values beyond the hysteresis loop. Specifically, along the forward scan direction (solid line), ρ_{xy} first quantizes at $h/3e^2$ for $-0.330 < D < -0.293 \text{ V nm}^{-1}$, and then switches to $-h/3e^2$ for $-0.290 < D < -0.270 \text{ V nm}^{-1}$. On the reverse scan (dashed line), ρ_{xy} first quantizes at $-h/3e^2$ for $-0.307 < D < -0.270 \text{ V nm}^{-1}$, and then switches to $h/3e^2$ for $-0.334 < D < -0.310 \text{ V nm}^{-1}$. Notably, opposite Chern numbers can coexist within the same scan direction of D , a feature distinct from previous reports [32]. This observation of opposite Chern numbers at different D values resembles recent findings of D -controlled chirality switching in rhombohedral graphene/h-BN moiré superlattices [33,37]. The underlying mechanism is a displacement-field-induced topological phase transition, in which D modulates the distribution of Berry curvature and changes the Chern number of the corresponding valley Chern band.

Displacement-field-induced Chern number switching in twisted (2 + 4) L graphene

We further demonstrate that in twisted rhombohedral graphene, the displacement field D can not only switch the sign but also alter the absolute value of the Chern number C . This capability is achieved by engineering the layer configuration of the twisted stack. As shown in Fig. 4, we observe in twisted (2 + 4) L graphene (device D4, $\theta = 1.21^\circ$) that D can drive a topological phase transition between a $C = 3$ QAH state and a $C = 4$ QAH state.

Figure 4b presents the $\nu - D$ map of symmetrized ρ_{xx} and anti-symmetrized ρ_{xy} at $B = \pm 90 \text{ mT}$. Similar to the twisted (1 + N) L graphene family, topologically nontrivial states emerge near $\nu = 1$, signaled by regions of anomalously large ρ_{xy} and vanishing ρ_{xx} . A distinct feature, however, is that the ρ_{xx} minima are split into two separate regions by a local maximum near $D \approx -0.628 \text{ V nm}^{-1}$. Meanwhile, the corresponding ρ_{xy} plateaus quantize to two different values. Figure 4f displays a linecut scan along red vertical line in Fig. 4b. Remarkably, ρ_{xy} is quantized at $h/3e^2$ for $-0.683 < D < -0.641 \text{ V nm}^{-1}$ and at $h/4e^2$ for $-0.608 < D < -0.571 \text{ V nm}^{-1}$.

Figure 4e shows ρ_{xy} and ρ_{xx} as a function of ν at two characteristic displacement fields $D = -0.669 \text{ V nm}^{-1}$ and $D = -0.602 \text{ V nm}^{-1}$, marked by violet and white horizontal lines in Fig. 4b, respectively. The quantization of ρ_{xy} and vanishing ρ_{xx} are consistent with Fig. 4f. Magnetic hysteresis measurements taken at the positions indicated by green and pink stars in Fig. 4b exhibit pronounced hysteresis loops, with precisely quantized $\rho_{xy} = h/3e^2$ and $\rho_{xy} = h/4e^2$ persisting down to zero magnetic field, respectively, confirming their QAH nature. The Chern numbers are further corroborated by Landau fan diagrams (Fig. 4g, h), whose slopes according to the Streda formula yield $C = 3$ and $C = 4$ at two selected D .

Although displacement-field-induced topological phase transitions have been theoretically proposed in various systems [20,44,50,51], their experimental realization in a QAH regime, specifically a transition between two distinct topologically nontrivial Chern states, has remained elusive. Our observation of a D -driven topological phase transition from $C = 3$ to $C = 4$ provides this demonstration and agrees well with band structure calculations, as shown in Fig. 4a.

Discussion and conclusion

Our observations of layer- and gate-tunable high- C QAH states in twisted rhombohedral graphene establish a versatile platform for both fundamental research in topological matter and future quantum device engineering. The realization of such states opens the door to exploring a rich hierarchy of correlated topological orders beyond the conventional Landau level paradigm. In particular, fractional Chern insulators in high- C Chern bands are promising candidates for hosting non-Abelian excitations, which are of central interest for topological quantum computation [52,53]. Already in our devices, we observe signatures of unconventional Chern insulators emerging at non-integer fillings, including an integer Chern insulator at $\nu = 3/2$ and indications of an incipient fractional Chern insulator at $\nu = 7/3$ in the twisted (1 + 3) L device (see Extended Data Fig. 8, 9). These topologically nontrivial states manifest as an anomalous Hall effect with magnetic hysteresis and dispersive fan diagrams. Although the corresponding ρ_{xy} fails to quantize at zero magnetic field, which we attribute to residual disorder or imperfect contact, our system provides a promising platform for approaching the appealing fractional Chern insulators in high- C Chern bands.

From the perspective of electronic applications, our work validates a design principle for topological band engineering: the Chern number can be programmed by selecting specific layer configurations, shifting the field from discovery-driven to design-driven research (see our prediction in Extended Data Fig. 10). This principle could be extended to create even higher Chern bands using thicker graphene stacks. Remarkably, the rich choice of QAH states with different C , when coupled with proximity-induced superconductivity, offers a route to engineer chiral Majorana edge modes. Furthermore, the ability to electrostatically switch between distinct Chern numbers in a single device introduces a novel mechanism for topological electronics. Such a device could function as a topological transistor, modulating the number of dissipationless edge channels via gate voltage alone.

Methods

Device fabrication

Our heterostructures consist of twisted monolayer (or bilayer) graphene and rhombohedral multilayer graphene, encapsulated by top and bottom h-BN dielectric layers, with few-layer graphite serving as the top and bottom gates. Graphite and h-BN flakes were mechanically exfoliated onto SiO_2/Si substrates from bulk crystals. The layer numbers of multilayer graphene were determined by optical contrast. Rhombohedral stacking domains were first identified using an infrared camera and then confirmed by Raman spectroscopy (see Extended Data Fig. 1). Monolayer (bilayer) and rhombohedral multilayer graphene regions were selected within the same flake and separated into individual pieces by atomic force microscope (AFM) lithography or ultrafast laser cutting. All stacks were assembled using a standard dry-transfer technique assisted by a poly (bisphenol A carbonate) (PC)/polydimethylsiloxane (PDMS) stamp. The transfer sequence was: topmost h-BN, top graphite, top h-BN, monolayer (bilayer) graphene, and finally the rhombohedral multilayer graphene at a controlled twist angle. The assembled stack was then released onto a prepared bottom stack consisting of bottom graphite and bottom h-BN, which has been cleaned by AFM in contact mode. The presence of rhombohedral stacking domains in the final stack was further verified by additional Raman mapping. AFM imaging was used to identify bubble-free regions for device fabrication. The stacks were then patterned into Hall bar geometries using standard electron-beam lithography followed by reactive-ion etching. Electrical contacts were made by depositing Cr/Au via electron-beam evaporation.

Device D3, which was fabricated with a metallic top gate and a graphite bottom gate, has been systematically studied previously [39]. All other devices in this study are newly fabricated with both top and bottom graphite gates.

Electrical transport measurements

Measurements were performed in a Helium-4 cryostat with a Helium-3 insert with a base temperature of 0.3 K (Oxford TeslatronPT, for devices D1 and D4) or in a dilution refrigerator with a base temperature of approximately 50 mK (Oxford Triton, for devices D2 and D3), unless otherwise specified. Standard low-frequency lock-in techniques (SR830 or Zurich Instruments MFLI) were employed to measure the longitudinal resistance R_{xx} and Hall resistance R_{xy} at an excitation frequency of 17.7 Hz with an ac current of 1 nA - 5 nA. Gate voltages were applied using Keithley 2614B or Keithley 2450 source-measure units.

The carrier density n and displacement field D in the devices were derived from the top- and bottom- gate voltages (V_t and V_b) via: $n = \frac{C_b V_b + C_t V_t}{e} - n_0$ and $D = \frac{C_b V_b - C_t V_t}{2\epsilon_0} - D_0$, where C_b and C_t

are the bottom- and top-gate capacitances calibrated from the quantum oscillations, e is the elementary charge, and ϵ_0 is the vacuum permittivity. The offsets n_0 and D_0 account for intrinsic doping and built-in electric field. The moiré filling factor ν is given by $\nu = 4n/n_s$, where $n_s = 4/A$ is the carrier density at full filling and A is the area of the moiré unit cell.

Throughout this work, positive D is defined as the electric field pointing from the rhombohedral multilayer graphene toward monolayer (bilayer) graphene, as illustrated in Fig. 1a.

Twisted angle determination

The twist angle θ was extracted from the carrier density n_s at full filling ($\nu = 4$) using the relation $n_s \approx 8\theta^2/\sqrt{3}a^2$, where $a = 0.246$ nm is the graphene lattice constant. Alternatively, θ was independently determined from Brown-Zak oscillations, where minima in R_{xx} occur at $B = \phi_0/qA$. Here, $\phi_0 = h/e$ is the flux quantum, q is an integer, and $A = \sqrt{3}\lambda^2/2$ is the moiré unit-cell area. Linear fitting of q versus $1/B$ yields the moiré wavelength λ , from which θ is calculated. The twist angles of all devices are summarized in Extended Data Tab. 1.

Symmetrization and anti-symmetrization

To eliminate geometric mixing between R_{xx} and R_{xy} , we applied standard symmetrization and anti-symmetrization procedures. For the data at fixed magnetic field B , we employed $R_{xx}(\pm B) = [R_{xx}(+B) + R_{xx}(-B)]/2$ and $R_{xy}(\pm B) = [R_{xy}(+B) - R_{xy}(-B)]/2$. For magnetic hysteresis loops, the following definitions were used: $R_{xy}^{\text{anti-sym}}(B, \leftarrow) = [R_{xy}^{\text{raw}}(B, \leftarrow) - R_{xy}^{\text{raw}}(-B, \rightarrow)]/2$, $R_{xy}^{\text{anti-sym}}(B, \rightarrow) = [R_{xy}^{\text{raw}}(B, \rightarrow) - R_{xy}^{\text{raw}}(-B, \leftarrow)]/2$, $R_{xx}^{\text{sym}}(B, \leftarrow) = [R_{xx}^{\text{raw}}(B, \leftarrow) + R_{xx}^{\text{raw}}(-B, \rightarrow)]/2$, and $R_{xx}^{\text{sym}}(B, \rightarrow) = [R_{xx}^{\text{raw}}(B, \rightarrow) + R_{xx}^{\text{raw}}(-B, \leftarrow)]/2$, where arrows indicate the scan direction of B . Resistivity were obtained as $\rho_{xx} = R_{xx}W/L$ and $\rho_{xy} = R_{xy}$, with W and L being the width and length of the Hall bar, respectively.

Band structure calculation based on continuum model

The single-particle band structure was calculated by using continuum model. Specifically, the Hamiltonian of twisted rhombohedral multilayer graphene is

$$\mathcal{H}_{\text{tot}} = \mathcal{H}_{m+n} + \mathcal{T} + V_{\text{ext}},$$

where $\mathcal{H}_{m+n} = h_{m,-\theta/2} + h_{n,\theta/2}$ is the Hamiltonian describing the twisted graphene formed by the bottom (m -layer) and top (n -layer) stacks, \mathcal{T} encodes the hopping processes between the bottom and top stacks, and V_{ext} describes the external displacement-field-induced potential on the each layer of twisted graphene. $h_{N,\phi}$ denotes the Hamiltonian of rotated rhombohedral N -layer graphene, with the rotation angle ϕ relative to the x -axis and constructed from Slonczewski-Weiss-McClure tight-binding lattice model. Mathematical details and physical parameters can be found in Supplementary Information.

Self-consistent Hartree-Fock calculation

The interacting band structure was calculated by further applying self-consistent Hartree-Fock method to the single-particle band structure. The Coulomb interaction Hamiltonian is given by

$$H^{\text{int}} = \frac{1}{2A} \sum_{\alpha, \alpha'} \sum_{\tilde{k}_1, \tilde{k}_2, \tilde{q}} V_{\alpha\alpha'}(\tilde{q}) c_{\alpha, \tilde{k}_1 + \tilde{q}}^\dagger c_{\alpha', \tilde{k}_2 - \tilde{q}}^\dagger c_{\alpha', \tilde{k}_2} c_{\alpha, \tilde{k}_1}$$

where A is the total area of the sample, $\alpha = A_1, \dots, B_{N_b+N_t}$ corresponds to the mixture of sublattice and layer indices, \tilde{k}, \tilde{q} are defined in the big Brillouin zone, and the dual gate-screened Coulomb potential

$$V_{\alpha\alpha'}(q) = \frac{e^2 \tanh(|q|d_s)}{2\epsilon_0 \epsilon_r |q|}$$

with the screening length $d_s = 53$ nm for (1 + 5) L and 28 nm for other configurations to emulate

the experiment and the relative dielectric constant $\epsilon_r = 20$. The first five conduction bands were used to calculate. The details can be found in Supplementary Information. Notably, in certain configurations and parameter regimes, the single-particle Hamiltonian alone yields an isolated, flat, and topologically nontrivial first conduction band. For completeness, we include Hartree–Fock terms in our calculations and find that the band topology remains unchanged.

Note added: During the preparation of this manuscript, we became aware of other complementary and independent studies on twisted Bernal bilayer-rhombohedral tetralayer graphene [54] and twisted monolayer-rhombohedral multilayer graphene family [55].

Data availability

The data that support the findings of this study are available from the corresponding author upon reasonable request.

Acknowledgements

This work was funded by National Natural Science Foundation of China (Grant No. 12550402, 12274354, 12574203, 12474144, and 22473099), the Zhejiang Provincial Natural Science Foundation of China (Grant No. LR24A040003 and XHD23A2001), and Westlake Education Foundation at Westlake University. We thank Chao Zhang from the Instrumentation and Service Center for Physical Sciences (ISCPs) at Westlake University for technical and facility support in data acquisition. We also thank the Instrumentation and Service Center for Molecular Sciences (ISCMS) at Westlake University for facility support. K.W. and T.T. acknowledge support from the JSPS KAKENHI (Grant Nos. 21H05233 and 23H02052) and World Premier International Research Center Initiative (WPI), MEXT, Japan.

Author contributions

S.X. conceived the idea and supervised the project. Z.C. and N.L. fabricated the devices with the assistance of H.X., W.Zhou, X.F., L.W., Q.C., and X.C.. Z.C. and N.L. performed transport measurements with the assistance of J.D. and W.Zhou. N.L., Z.C., N.X., W.Zhu, and S.X. performed data analysis. J.H. and W.Zhu calculated the band structure. K.W. and T.T. grew h-BN crystals. N.L., C.Z., J.H., W.Zhu, and S.X. wrote the manuscript. All authors contributed to the discussions.

References

1. F. D. M. Haldane. Model for a quantum Hall effect without Landau levels: condensed-matter realization of the "parity anomaly". *Phys. Rev. Lett.* **61**, 2015-2018, (1988).
2. C.-Z. Chang *et al.* Experimental observation of the quantum anomalous Hall effect in a magnetic topological insulator. *Science* **340**, 167-170, (2013).
3. C.-Z. Chang, C.-X. Liu & A. H. MacDonald. Colloquium: Quantum anomalous Hall effect. *Rev. Mod. Phys.* **95**, 011002, (2023).
4. Y.-F. Wang, H. Yao, C.-D. Gong & D. N. Sheng. Fractional quantum Hall effect in topological flat bands with Chern number two. *Phys. Rev. B* **86**, 201101, (2012).
5. S. Yang, Z.-C. Gu, K. Sun & S. Das Sarma. Topological flat band models with arbitrary Chern numbers. *Phys. Rev. B* **86**, 241112, (2012).
6. Z. Liu, E. J. Bergholtz, H. Fan & A. M. Läuchli. Fractional Chern insulators in topological flat bands with higher Chern number. *Phys. Rev. Lett.* **109**, 186805, (2012).
7. G. Möller & N. R. Cooper. Fractional Chern insulators in Harper-Hofstadter bands with higher Chern number. *Phys. Rev. Lett.* **115**, 126401, (2015).
8. J. Ge *et al.* High-Chern-number and high-temperature quantum Hall effect without Landau levels. *Natl. Sci. Rev.* **7**, 1280-1287, (2020).
9. Y. Deng *et al.* Quantum anomalous Hall effect in intrinsic magnetic topological insulator MnBi₂Te₄. *Science* **367**, 895-900, (2020).
10. Z. Lian *et al.* Antiferromagnetic quantum anomalous Hall effect under spin flips and flops. *Nature* **641**, 70-75, (2025).
11. M. Serlin *et al.* Intrinsic quantized anomalous Hall effect in a moiré heterostructure. *Science* **367**, 900-903, (2020).
12. T. Li *et al.* Quantum anomalous Hall effect from intertwined moiré bands. *Nature* **600**, 641-646, (2021).
13. H. Park *et al.* Observation of fractionally quantized anomalous Hall effect. *Nature* **622**, 74-79, (2023).
14. F. Xu *et al.* Observation of integer and fractional quantum anomalous Hall effects in twisted bilayer MoTe₂. *Phys. Rev. X* **13**, 031037, (2023).
15. Z. Lu *et al.* Fractional quantum anomalous Hall effect in multilayer graphene. *Nature* **626**, 759-764, (2024).
16. R. Su *et al.* Moiré-driven topological electronic crystals in twisted graphene. *Nature* **637**, 1084-1089, (2025).
17. Y.-F. Zhao *et al.* Tuning the Chern number in quantum anomalous Hall insulators. *Nature* **588**, 419-423, (2020).
18. F. Zhang, J. Jung, G. A. Fiete, Q. Niu & A. H. MacDonald. Spontaneous quantum Hall states in chirally stacked few-layer graphene systems. *Phys. Rev. Lett.* **106**, 156801, (2011).
19. B. L. Chittari, G. Chen, Y. Zhang, F. Wang & J. Jung. Gate-tunable topological flat bands in trilayer graphene boron-nitride moiré superlattices. *Phys. Rev. Lett.* **122**, 016401, (2019).
20. Y. Park, Y. Kim, B. L. Chittari & J. Jung. Topological flat bands in rhombohedral tetralayer and multilayer graphene on hexagonal boron nitride moiré superlattices. *Phys. Rev. B* **108**, 155406, (2023).
21. M. Koshino. Interlayer screening effect in graphene multilayers with ABA and ABC stacking. *Phys. Rev. B* **81**, 125304, (2010).

22. N. B. Kopnin, T. T. Heikkilä & G. E. Volovik. High-temperature surface superconductivity in topological flat-band systems. *Phys. Rev. B* **83**, 220503, (2011).
23. G. Chen *et al.* Tunable correlated Chern insulator and ferromagnetism in a moiré superlattice. *Nature* **579**, 56-61, (2020).
24. T. Han *et al.* Orbital multiferroicity in pentalayer rhombohedral graphene. *Nature* **623**, 41-47, (2023).
25. J. Ding *et al.* Spin-Orbit-Driven Quarter Semimetals in Rhombohedral Graphene. *Adv. Mater.*, e12713, (2025).
26. Y. Shi *et al.* Electronic phase separation in multilayer rhombohedral graphite. *Nature* **584**, 210-214, (2020).
27. W. Zhou *et al.* Layer-polarized ferromagnetism in rhombohedral multilayer graphene. *Nat. Commun.* **15**, 2597, (2024).
28. T. Han *et al.* Large quantum anomalous Hall effect in spin-orbit proximitized rhombohedral graphene. *Science* **384**, 647-651, (2024).
29. Y. Sha *et al.* Observation of a Chern insulator in crystalline ABCA-tetralayer graphene with spin-orbit coupling. *Science* **384**, 414-419, (2024).
30. J. Xie *et al.* Tunable fractional Chern insulators in rhombohedral graphene superlattices. *Nat. Mater.* **24**, 1042-1048, (2025).
31. Z. Lu *et al.* Extended quantum anomalous Hall states in graphene/hBN moiré superlattices. *Nature* **637**, 1090–1095, (2025).
32. Y. Choi *et al.* Superconductivity and quantized anomalous Hall effect in rhombohedral graphene. *Nature* **639**, 342–347, (2025).
33. J. Ding *et al.* Electric-field switchable chirality in rhombohedral graphene Chern insulators stabilized by tungsten diselenide. *Phys. Rev. X* **15**, 011052, (2025).
34. P. J. Ledwith, A. Vishwanath & E. Khalaf. Family of ideal Chern flatbands with arbitrary Chern number in chiral twisted graphene multilayers. *Phys. Rev. Lett.* **128**, 176404, (2022).
35. J. Liu, Z. Ma, J. Gao & X. Dai. Quantum valley Hall effect, orbital magnetism, and anomalous Hall effect in twisted multilayer graphene systems. *Phys. Rev. X* **9**, 031021, (2019).
36. J. Wang & Z. Liu. Hierarchy of ideal flatbands in chiral twisted multilayer graphene models. *Phys. Rev. Lett.* **128**, 176403, (2022).
37. Q. Liu *et al.* Odd-Chern-number quantum anomalous Hall effect at even filling in moiré rhombohedral heptalayer graphene. *Phys. Rev. Lett.* **136**, 016602, (2026).
38. H. Xiang *et al.* Continuously tunable anomalous Hall crystals in rhombohedral heptalayer graphene. arXiv:2502.18031, (2025).
39. N. Liu *et al.* Diverse high-Chern-number quantum anomalous Hall insulators in twisted rhombohedral graphene. arXiv:2507.11347, (2025).
40. J. Dong *et al.* Observation of Integer and fractional Chern insulators in high Chern number flatbands. arXiv:2507.09908, (2025).
41. W. Wang *et al.* Programmable quantum anomalous Hall insulator in twisted crystalline flatbands. arXiv:2507.10875, (2025).
42. Y. Cao *et al.* Unconventional superconductivity in magic-angle graphene superlattices. *Nature* **556**, 43-50, (2018).
43. K. Kim *et al.* van der Waals heterostructures with high accuracy rotational alignment. *Nano Lett.* **16**, 1989-1995, (2016).

44. Y.-H. Zhang, D. Mao, Y. Cao, P. Jarillo-Herrero & T. Senthil. Nearly flat Chern bands in moiré superlattices. *Phys. Rev. B* **99**, 075127, (2019).
45. C. Wu. Orbital analogue of the quantum anomalous Hall effect in *p*-band systems. *Phys. Rev. Lett.* **101**, 186807, (2008).
46. M. Koshino & E. McCann. Trigonal warping and Berry's phase $N\pi$ in ABC-stacked multilayer graphene. *Phys. Rev. B* **80**, 165409, (2009).
47. H. Polshyn *et al.* Topological charge density waves at half-integer filling of a moiré superlattice. *Nat. Phys.* **18**, 42-47, (2022).
48. H. Polshyn *et al.* Electrical switching of magnetic order in an orbital Chern insulator. *Nature* **588**, 66-70, (2020).
49. J. Zhu, J. J. Su & A. H. MacDonald. Voltage-controlled magnetic reversal in orbital Chern insulators. *Phys. Rev. Lett.* **125**, 227702, (2020).
50. S. Zhang, X. Dai & J. Liu. Spin-polarized nematic order, quantum valley Hall states, and field-tunable topological transitions in twisted multilayer graphene systems. *Phys. Rev. Lett.* **128**, 026403, (2022).
51. W. Liang *et al.* Chern number tunable quantum anomalous Hall effect in compensated antiferromagnets. *Phys. Rev. Lett.* **134**, 116603, (2025).
52. C. Nayak, S. H. Simon, A. Stern, M. Freedman & S. Das Sarma. Non-Abelian anyons and topological quantum computation. *Rev. Mod. Phys.* **80**, 1083-1159, (2008).
53. A. Sterdyniak, C. Repellin, B. A. Bernevig & N. Regnault. Series of Abelian and non-Abelian states in $C>1$ fractional Chern insulators. *Phys. Rev. B* **87**, 205137, (2013).
54. Z. Li *et al.* Fractionalization and entanglement of high Chern insulators. arXiv:2512.21612, (2025).
55. X. Wang *et al.* Family of high-Chern-number orbital magnets in twisted rhombohedral graphene. arXiv:2601.01087, (2026).

Figures

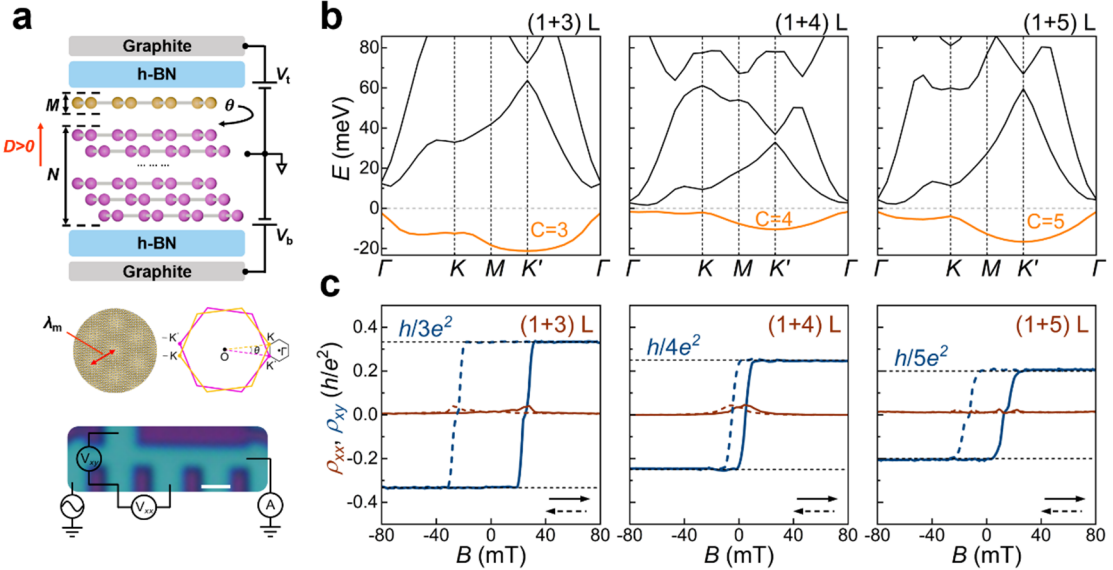


Fig. 1 | Layer-dependent QAH effect in twisted monolayer-rhombohedral multilayer graphene family. **a**, Device schematic with dual graphite gates. A moiré superlattice forms between monolayer (or bilayer) graphene and rhombohedral multilayer graphene with a twist angle θ . The D is defined as positive when pointing from the rhombohedral graphene toward monolayer (bilayer) graphene. Bottom panel shows optical image of a final device with scale bar of $1 \mu\text{m}$. **b**, Calculated band structures of twisted $(1 + N)$ L graphene based on self-consistent Hartree-Fock method. Energies are measured with respect to the Fermi level. The twist angles (interlayer potential differences) used in the calculation are $\theta = 1.29^\circ$ ($\Delta = 9.0$ meV), $\theta = 1.16^\circ$ ($\Delta = 12.5$ meV), $\theta = 1.39^\circ$ ($\Delta = 11.0$ meV) for $N = 3, 4, 5$, respectively (see details in Methods). In each case, the first conduction band is an isolated Chern band with the valley Chern number C , which coincides with the layer number N . **c**, Magnetic hysteresis of symmetrized ρ_{xx} and anti-symmetrized ρ_{xy} as a function of B swept forward and backward at $\nu = 1$ for twisted $(1 + N)$ L graphene devices with $N = 3$ (device D1, $D = -0.470 \text{ V nm}^{-1}$), $N = 4$ (device D2, $D = -0.508 \text{ V nm}^{-1}$), and $N = 5$ (device D3, $D = -0.620 \text{ V nm}^{-1}$). Data were taken at $T = 0.3 \text{ K}$ for device D1 and $T = 50 \text{ mK}$ for device D2 and D3.

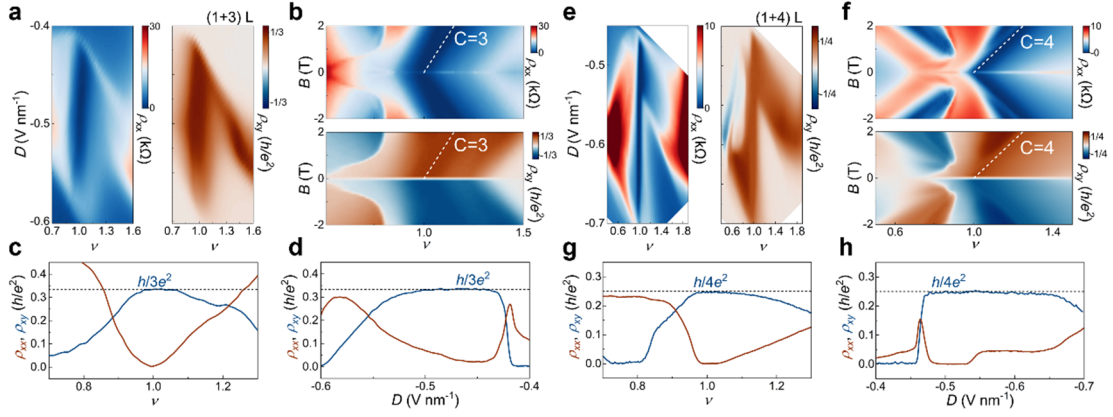


Fig. 2 | QAH effects with $C = 3$ ($C = 4$) at $v = 1$ in twisted $(1 + 3)$ L ($(1 + 4)$ L) graphene. **a-d**, Data from twisted $(1 + 3)$ L graphene device (device D1, $\theta = 1.29^\circ$) measured at $T = 0.3$ K. **a**, Symmetrized ρ_{xx} (left) and anti-symmetrized ρ_{xy} (right) as functions of v and D measured at $B = \pm 0.1$ T. **b**, Landau fan diagrams of symmetrized ρ_{xx} (top) and anti-symmetrized ρ_{xy} (bottom) at fixed $D = -0.470$ V nm $^{-1}$. White dashed lines trace the dispersions of the minima in ρ_{xx} and plateaus in ρ_{xy} . Their slope gives $C = 3$ via the Streda formula. **c, d**, Symmetrized ρ_{xx} and anti-symmetrized ρ_{xy} versus v at fixed $D = -0.470$ V nm $^{-1}$ (**c**) and versus D at fixed $v = 1$ (**d**) measured at $B = \pm 50$ mT. Black dashed lines mark the quantized plateaus $\rho_{xy} = h/3e^2$. **e-h**, Corresponding data from twisted $(1 + 4)$ L graphene device (device D2, $\theta = 1.16^\circ$) measured at $T = 50$ mK. **e**, Symmetrized ρ_{xx} (left) and anti-symmetrized ρ_{xy} (right) versus v and D measured at $B = \pm 90$ mT. **f**, Landau fans of symmetrized ρ_{xx} (top) and anti-symmetrized ρ_{xy} (bottom) at fixed $D = -0.508$ V nm $^{-1}$. White dashed lines yield $C = 4$. **g, h**, Symmetrized ρ_{xx} and anti-symmetrized ρ_{xy} versus v at fixed $D = -0.508$ V nm $^{-1}$ (**g**) and versus D at fixed $v = 1$ (**h**) measured at $B = \pm 90$ mT. Black dashed lines indicate the quantized plateaus $\rho_{xy} = h/4e^2$.

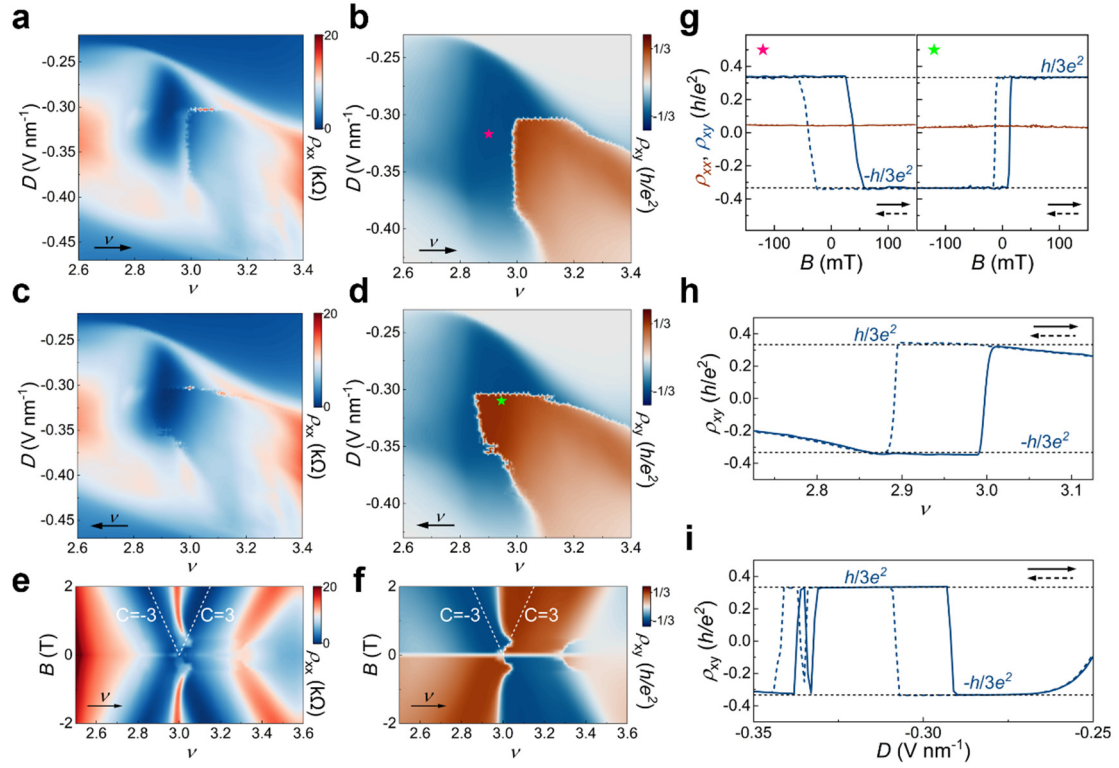


Fig. 3 | Electrically switchable chirality of QAH states near $\nu = 3$ in twisted (1 + 3) L graphene. **a, b**, ρ_{xx} (**a**) and ρ_{xy} (**b**) as functions of ν and D with ν swept forward measured at $B = 0.1$ T. **c, d**, Corresponding maps with ν swept backward. **e, f**, Landau fan diagrams of symmetrized ρ_{xx} (**e**) and anti-symmetrized ρ_{xy} (**f**) at fixed $D = -0.317$ V nm⁻¹. White dashed lines trace the dispersions of ρ_{xx} minima and ρ_{xy} plateaus, yielding two Chern states of $C = 3$ and $C = -3$ via the Streda formula. **g**, Magnetic hysteresis of symmetrized ρ_{xx} and anti-symmetrized ρ_{xy} as a function of B swept forward and backward measured at the positions marked by the pink star ($\nu = 2.905$ and $D = -0.317$ V nm⁻¹, left panel) and green star ($\nu = 2.947$ and $D = -0.310$ V nm⁻¹, right panel) in (**b**) and (**d**), respectively. **h**, ρ_{xy} as a function of ν swept forward and backward at fixed $D = -0.317$ V nm⁻¹ and $B = 0.1$ T. **i**, ρ_{xy} as a function of D swept forward and backward at fixed $\nu = 2.947$ and $B = 0.1$ T. Black dashed lines in (**h**) and (**i**) mark the quantized plateaus $\rho_{xy} = \pm h/3e^2$. All data were acquired from device D1 at $T = 0.3$ K.

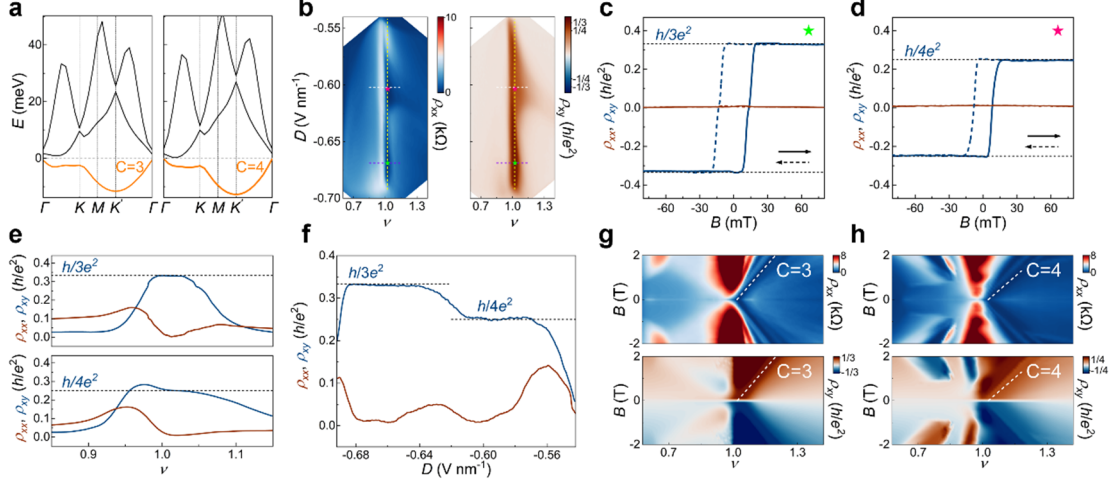
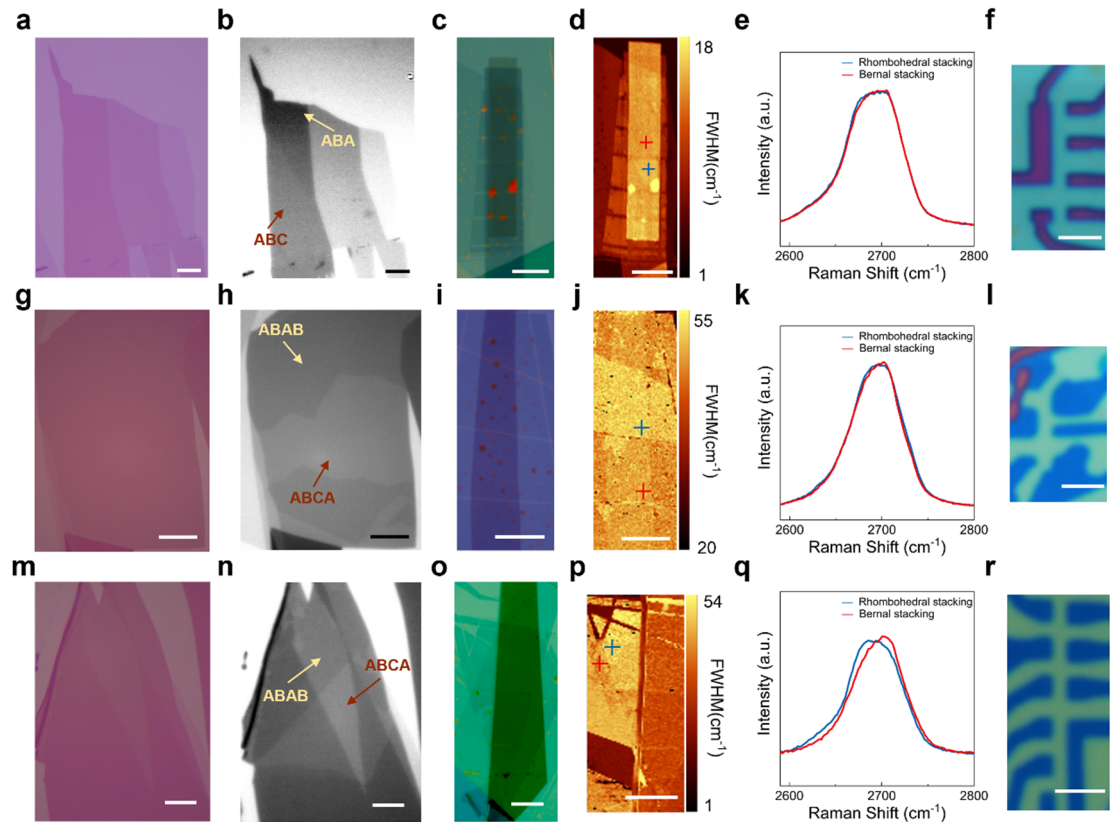
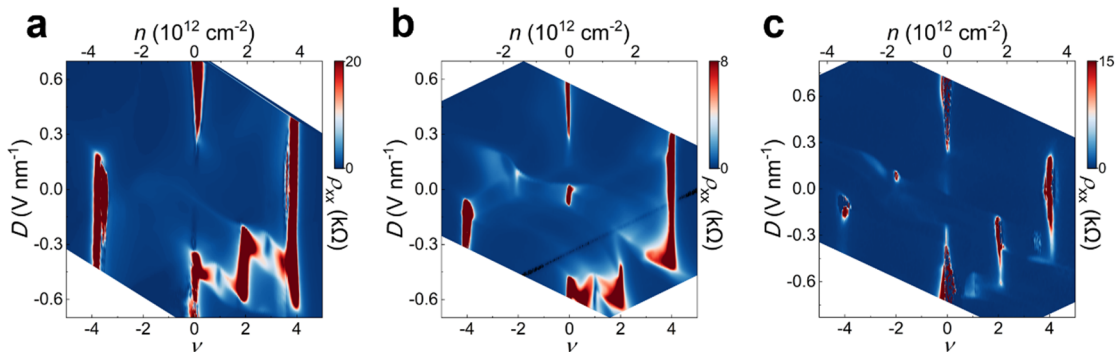


Fig. 4 Displacement-field-induced topological phase transition at $\nu = 1$ in twisted (2 + 4) L graphene. **a**, Self-consistent Hartree-Fock band structures under interlayer potential differences $\Delta = 11.5$ meV (left) and $\Delta = 10.0$ meV (right). **b**, Symmetrized ρ_{xx} (left) and anti-symmetrized ρ_{xy} (right) versus ν and D measured at $B = \pm 90$ mT. **c**, **d**, Magnetic hysteresis of symmetrized ρ_{xx} and anti-symmetrized ρ_{xy} as a function of B swept forward and backward measured at the green star ($\nu = 1.02$ and $D = -0.669$ V nm $^{-1}$) (**c**) and pink star ($\nu = 1.02$ and $D = -0.603$ V nm $^{-1}$) (**d**) marked in (**b**). **e**, ρ_{xx} and ρ_{xy} versus ν at fixed $D = -0.669$ V nm $^{-1}$ (top, violet line in **b**) and $D = -0.602$ V nm $^{-1}$ (bottom, white line in **b**) measured at $B = \pm 90$ mT. **f**, ρ_{xx} and ρ_{xy} versus D at fixed $\nu = 1.02$ measured at $B = \pm 90$ mT. Data were measured along yellow vertical line indicated in (**b**). Black dashed lines in (**e**) and (**f**) mark the quantized plateaus corresponding to $h/3e^2$ or $h/4e^2$. **g**, **h**, Landau fan diagrams of ρ_{xx} (top) and ρ_{xy} (bottom) at fixed $D = -0.669$ V nm $^{-1}$ (**g**) and $D = -0.602$ V nm $^{-1}$ (**h**). White dashed lines yield $C = 3$ (**g**) and $C = 4$ (**h**) via the Streda formula. All data were acquired from device D4 at $T = 0.3$ K.

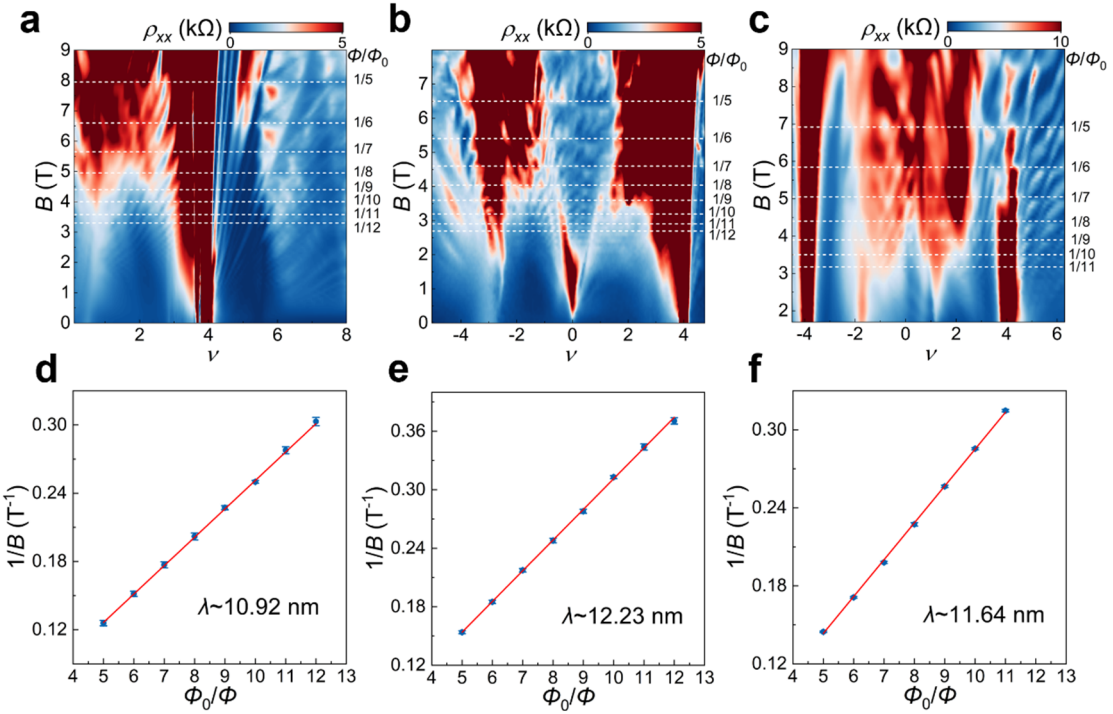
Extended Data Figures



Extended Data Fig. 1 | Optical Images and Raman characterization of twisted rhombohedral graphene devices. **a-f**, Data for twisted (1 + 3) L graphene (device D1). **g-l**, Data for twisted (1 + 4) L graphene (device D2). **m-r**, Data for twisted (2 + 4) L graphene (device D4). **a, b, g, h, m, n**, Optical and corresponding infrared images of rhombohedral trilayer (**a, b**) and tetralayer (**g, h, m, n**) graphene before laser cutting. The Bernal- and rhombohedral-stacking domains in panels (**b**), (**h**), and (**n**) are indicated by yellow and red arrows, respectively. **c, d, i, j, o, p**, Optical images (**c, i, o**) and Raman maps (**d, j, p**) of the final stacks. **e, k, q**, Raman spectra of the 2D peak taken at the red and blue crosses in (**d**), (**j**), and (**p**). **f, l, r**, Optical images of completed devices. Scale bars: 10 μ m in (**a-d, g-j, m-p**); 2 μ m (**f, l, r**).

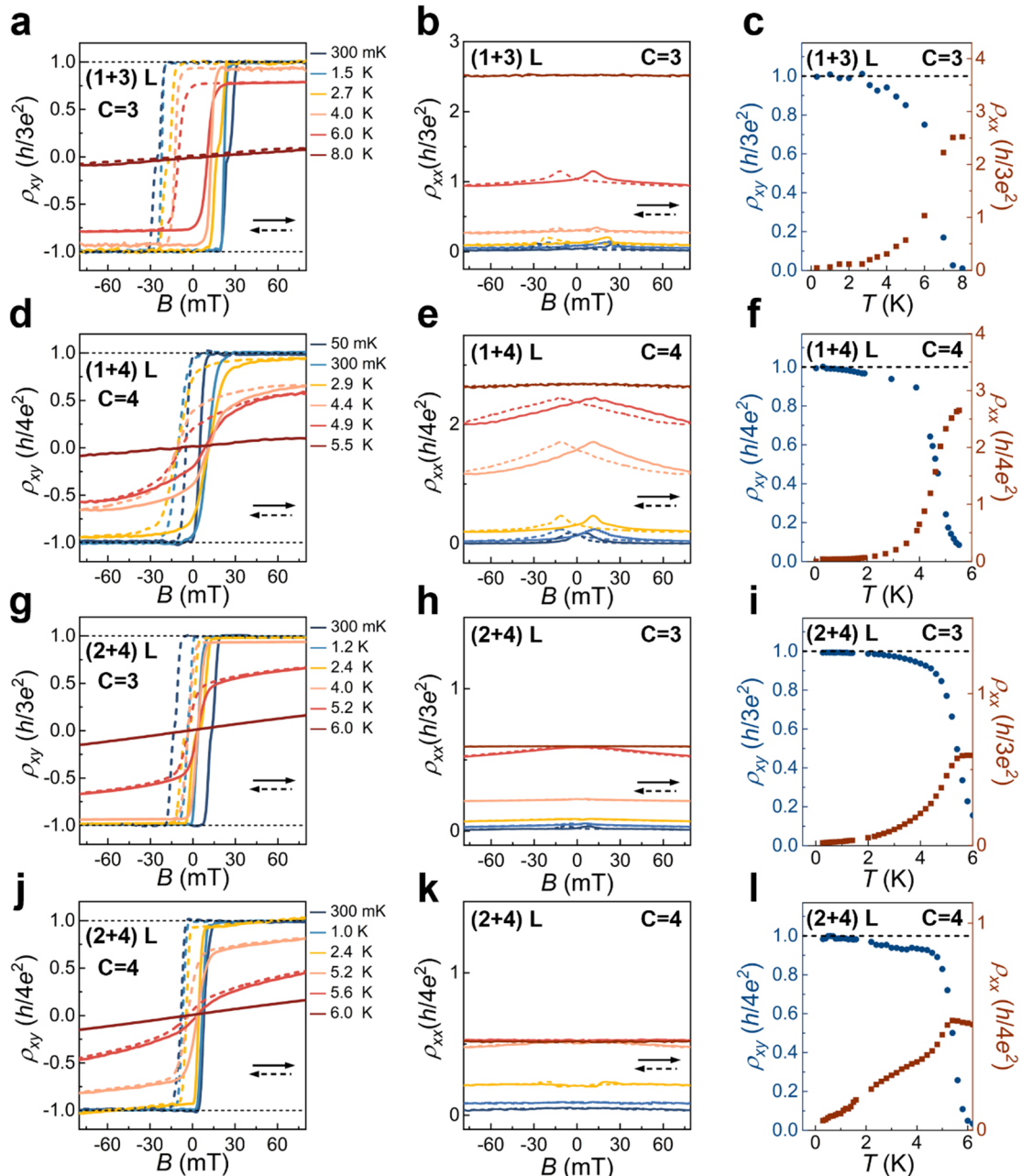


Extended Data Fig. 2 | Full ν - D maps at zero magnetic field. **a-c**, ρ_{xx} versus ν and D measured at $T = 0.3$ K for twisted (1 + 3) L graphene (device D1, **a**), twisted (1 + 4) L graphene (device D2, **b**), twisted (2 + 4) L graphene (device D4, **c**).

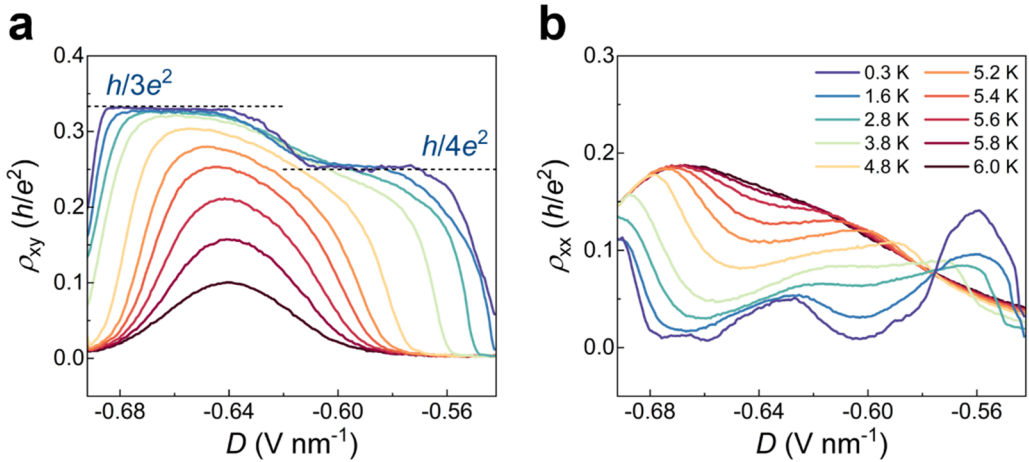


Extended Data Fig. 3 | Determination of moiré wavelength via Brown-Zak oscillations.

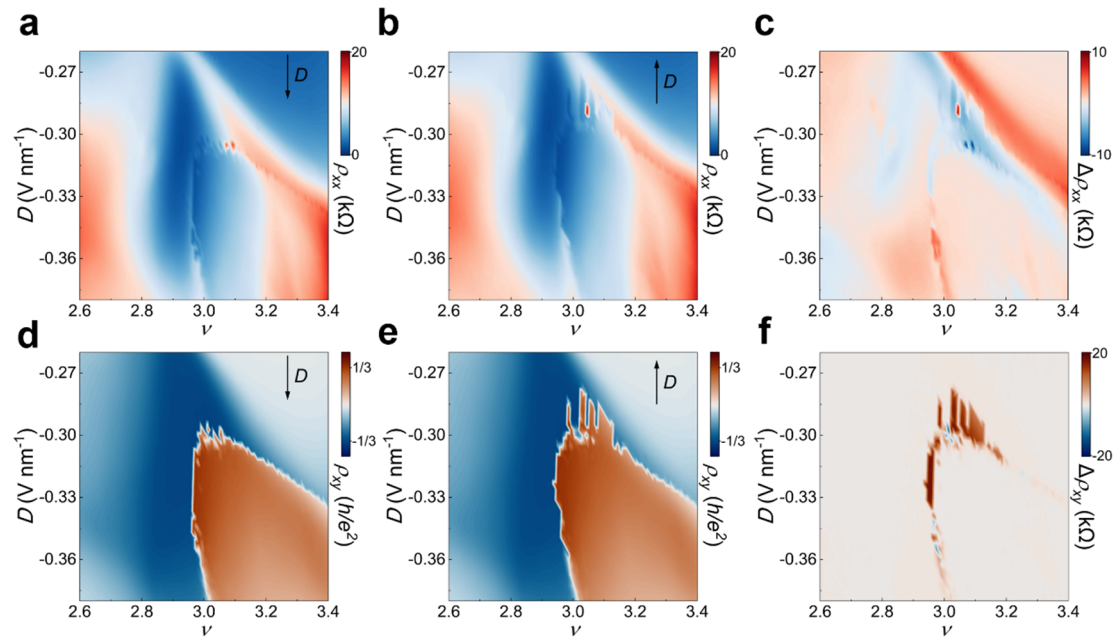
a-c, Landau fans of ρ_{xx} versus ν and B for device D1 at $D = -0.100$ V nm⁻¹ (**a**), device D2 at $D = 0.200$ V nm⁻¹ (**b**), and device D4 at $D = -0.100$ V nm⁻¹ (**c**). Horizontal dashed lines mark minima in Brown-Zak oscillations, which occur when the magnetic flux through the moiré unit cell satisfies $\phi = \phi_0/q$ with an integer q . **d-f**, Linear fits of $1/B$ at the oscillation minima versus ϕ_0/ϕ . The extracted moiré wavelengths are 10.92 nm (**d**), 12.23 nm (**e**), and 11.64 nm (**f**), corresponding to $\theta \approx 1.29^\circ$, $\theta \approx 1.16^\circ$, and $\theta \approx 1.21^\circ$ for device D1, device D2, and device D4, respectively.



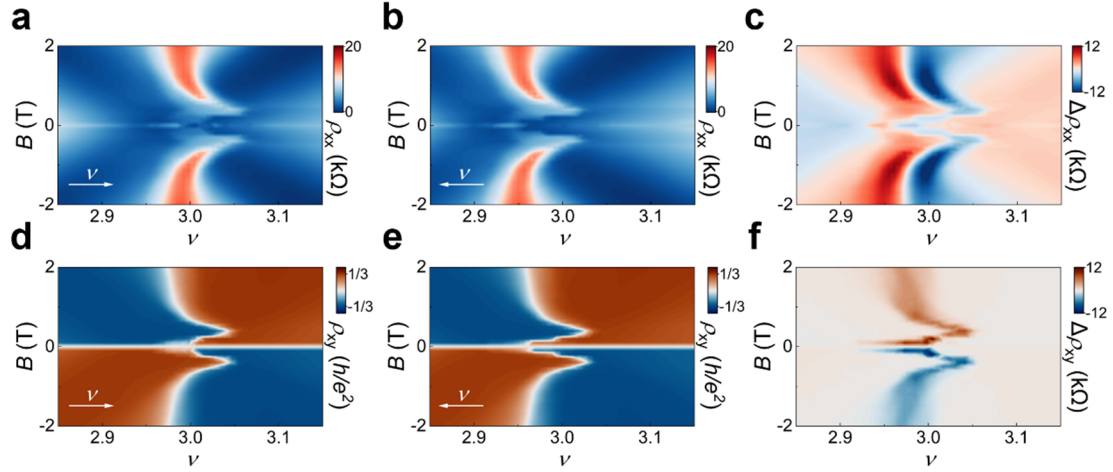
Extended Data Fig. 4 | Temperature dependence of the QAH states. **a-c**, Data for the $C = 3$ state at $\nu = 1$ in device D1. **d-f**, Data for $C = 4$ state at $\nu = 1$ in device D2. **g-i**, Data for $C = 3$ state at $\nu = 1$ in device D4. **j-l**, Data for $C = 4$ state at $\nu = 1$ in device D4. **a, b, d, e, g, h, j, k**, Magnetic hysteresis of ρ_{xx} (**a, d, g, j**) and ρ_{xy} (**b, e, h, k**) at selected temperatures. **c, f, i, l**, Extracted ρ_{xx} and ρ_{xy} as a function of temperature.



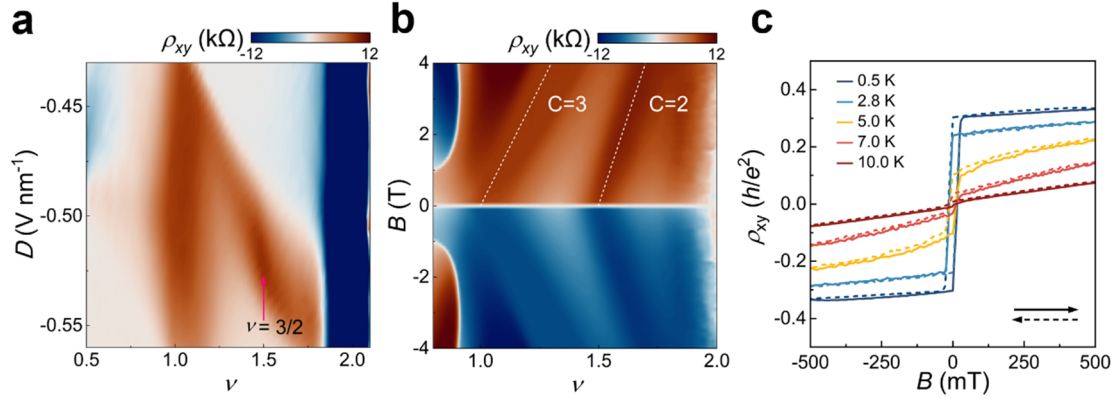
Extended Data Fig. 5 | Temperature dependence of topological phase transition in device D4.
a, b, symmetrized ρ_{xx} (a) and anti-symmetrized ρ_{xy} (b) versus D at fixed $\nu = 1.02$ measured at selected temperatures ($B = \pm 90$ mT).



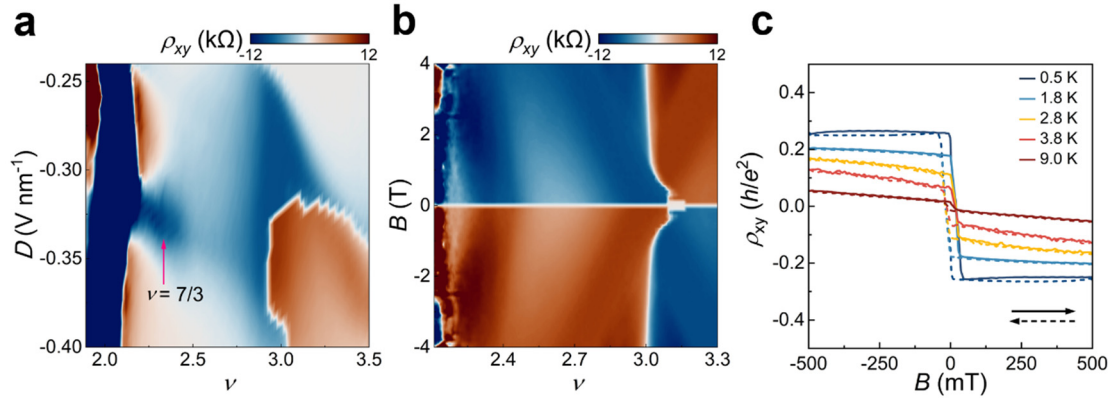
Extended Data Fig. 6 | Displacement-field-scan dependence of QAH states near $\nu = 3$ in twisted (1 + 3) L graphene (device D1). **a, b**, ρ_{xx} versus ν and D with D scanned downward (a) and upward (b), measured at $B = 0.1$ T. **c**, Difference map of ρ_{xx} between (a) and (b). **d, e**, Corresponding maps of ρ_{xy} with D scanned downward (d) and upward (e). **f**, Difference map of ρ_{xy} between (d) and (e).



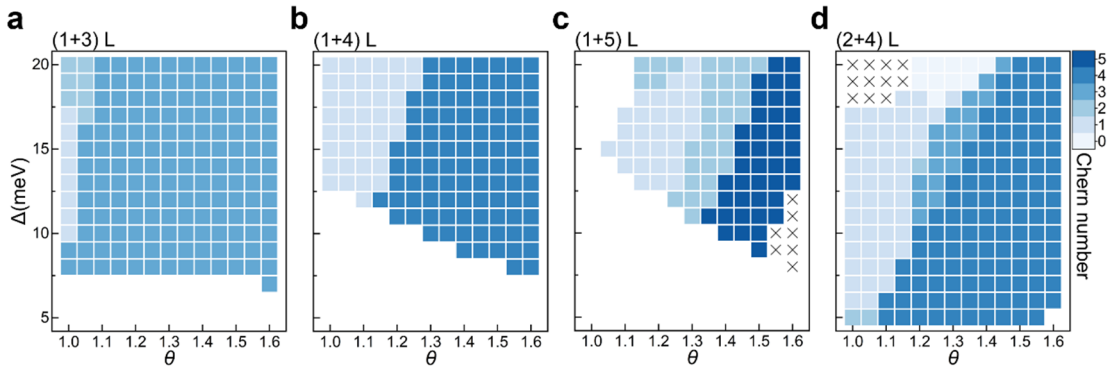
Extended Data Fig. 7 | Scan-direction-dependent Landau fans near $\nu = 3$ in twisted (1 + 3) L graphene (device D1) at $D = -0.317 \text{ V nm}^{-1}$. **a, b**, ρ_{xx} versus ν and B with ν scanned forward (**a**) and backward (**b**). **c**, Difference map of ρ_{xx} between (**a**) and (**b**). **d, e**, Corresponding maps of ρ_{xy} with ν scanned forward (**d**) and backward (**e**). **f**, Difference map of ρ_{xy} between (**d**) and (**e**).



Extended Data Fig. 8 | Unconventional Chern insulator at $\nu = 3/2$ in twisted (1 + 3) L graphene (device D1). **a**, ρ_{xy} versus ν and D measured at $B = \pm 0.1 \text{ T}$. **b**, Landau fan diagram of ρ_{xy} versus ν and B at $D = -0.520 \text{ V nm}^{-1}$. **c**, Magnetic hysteresis of ρ_{xy} versus B at $\nu = 3/2$ and $D = -0.520 \text{ V nm}^{-1}$ at selected temperatures.



Extended Data Fig. 9 | Incipient fractional Chern insulator near $\nu = 7/3$ in twisted $(1+3)$ L graphene (device D1). **a**, ρ_{xy} as a function of ν and D measured at $B = \pm 0.1$ T. **b**, Landau fan diagram of ρ_{xy} versus ν and B at $D = -0.330$ V nm $^{-1}$. **c**, Magnetic hysteresis of ρ_{xy} versus B near $\nu = 7/3$ and $D = -0.330$ V nm $^{-1}$ at selected temperatures.



Extended Data Fig. 10 | Calculated valley Chern numbers evolved with twist angle and interlayer potential difference for various layer configurations. **a-d**, The Chern numbers of the first conduction band as functions of twist angle θ and interlayer potential difference Δ for twisted $(1+3)$ L **(a)**, $(1+4)$ L **(b)**, $(1+5)$ L **(c)**, and $(2+4)$ L **(d)** graphene. All results are obtained from self-consistent Hartree-Fock calculations based on the continuum model. Data marked by ‘ \times ’ represent a gapless state under given parameters.

Extended Data Tab. 1 | Summary of measured devices.

Device	Layer (M+N)	Twist angle determined by full filling (°)	Moiré wavelength determined by full filling (nm)	Twist angle determined by Brown-Zak oscillations (°)	Moiré wavelength determined by Brown-Zak oscillations (nm)	Observed Chern number
D1	1+3	1.29	10.92	1.29	10.92	3, -3
D2	1+4	1.15	12.26	1.16	12.23	4
D3	1+5	1.40	10.07	1.39	10.14	5
D4	2+4	1.21	11.64	1.21	11.64	3, 4